Ocean Dynamics (2019) 69:581–597
https://doi.org/10.1007/s10236-019-01256-4

Extreme bed shear stress during coastal downwelling

Jochen Kämpf[1]

Received: 12 September 2018 / Accepted: 7 February 2019 / Published online: 18 March 2019

Abstract
The wind-driven circulation of coastal oceans has been studied for many decades. Using a 2.5-dimensional hydrodynamic model, this work unravels new aspects inherent with this circulation. In agreement with previous studies, downwelling-favorable coastal winds create an overturning cross-shelf circulation that operates to mix nearshore water. On timescales of days, this circulation tends to eliminate itself causing a "shutdown" of the cross-shelf circulation. For the first time, here, the author demonstrates that this shutdown is accompanied by creation of a zone of extremely high bed shear stresses (> 0.35 Pa) that operates to "plow" the seabed over an offshore distance of ~ 10–20 km. The author postulates that the associated sediment erosion episodes and their likely ammonification of the water column are key in the understanding of the biogeochemistry shaping coastal marine ecosystems.

Keywords Bed shear stress · Coastal oceanography · Coastal downwelling · Process-oriented hydrodynamic modelling

1 Introduction

In focus of this study are two important aspects of the seawater dynamics in shelf seas: (1) currents involved in the cross-shelf exchange of dissolved and particulate matter and (2) physical processes leading to the erosion of seabed sediment. Both aspects are intrinsically linked with the marine ecosystem dynamics through lateral advection and benthic release of nutrients. To this end, this work revisits the classical problem of the circulation and turbulence in coastal oceans that follows from longshore winds, which was first mathematically explored by V. Wilfrid Ekman (Ekman 1905). Based on the method of process-oriented modeling, this work reveals that downwelling-favorable winds can create a zone of extremely high bed shear stresses (> 0.35 Pa), which makes this situation a prime agent of seabed erosion.

It is well established that the cross-shelf circulation in deeper regions (> 10 m) of the continental shelf is driven by longshore winds on timescales of synoptic weather patterns (~ 3–10 days). The most studied process facilitating cross-shelf exchanges of water masses is that of classical wind-driven coastal upwelling (Fig. 1a) (see Kämpf and Chapman 2016). Upwelling follows from longshore wind stress driving surface water offshore in a surface Ekman layer. Consequently, the coastal sea level drops by several centimeters which initiates the creation of a swift geostrophic along-shelf jet. In turn, this jet forms a bottom Ekman layer via frictional effects within which near-bottom water is eventually moved shoreward and upward into the euphotic zone where it can fuel primary production. Early two-dimensional modeling studies indicate that this cross-shelf circulation extends close to the shore (Allen et al. 1995). The upwelling process creates a surface front—known as upwelling front—that gradually moves farther offshore due to the surface Ekman drift. The speed of the frontal current decreases with depth due horizontal density gradients, i.e., the thermal wind balance.

Downwelling follows from a coastal wind in the opposite direction; i.e., blowing with the coast on the right in the northern hemisphere (Fig. 1b). Early modeling studies (Allen and Newberger 1996) suggest that onshore flow in the surface Ekman layer creates a submerged subsurface front (characterized by locally enhanced downwelling flows) that has little density stratification on its landward side with essentially no cross-shelf circulation (Allen and Newberger 1996). Field observations from the North Carolina Shelf by Lentz (2001) provide strong observational evidence in support of such "shutdown" of the cross-shelf circulation in conjunction with

Responsible Editor: Dirk Olbers

✉ Jochen Kämpf
jochen.kaempf@flinders.edu.au

[1] College of Science and Engineering, Flinders University, PO Box 5100, Adelaide, SA 5001, Australia

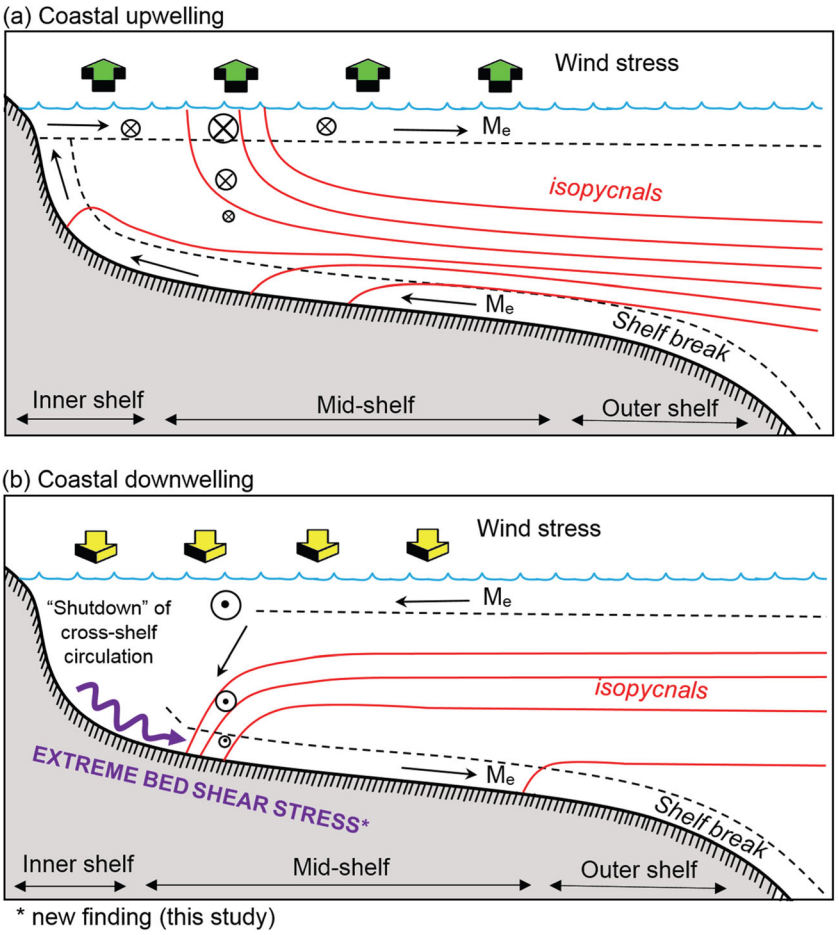

Fig. 1 Schematic representation of currents and modifications of the density field during episodes of **a** full coastal upwelling and **b** coastal downwelling. See the text for more details. Continental influences from river runoff are not considered here

an unstratified water column (Fig. 2). Wijesekera et al. (2003) reproduced the shutdown of the cross-shelf circulation in a sigma-coordinate model with the use of three different turbulence-closure schemes. In summary, previous hydrodynamic modeling studies indicate that the weakening of the cross-shelf circulation is affiliated with locally enhanced turbulent diffusion of momentum and matter.

Field observations from the North Carolina Shelf serve as a central reference for the simulations results presented here. The observations period included a storm, ~ 4 days in duration, with persistent and strong downwelling-favorable winds of ~ 0.3 Pa (Fig. 2a). Prior to the storm, the water column was relatively strongly stratified with density differences through the water column of $\Delta\rho \sim 1$–5 kg/m^3 (see Lentz 2001) with top-to-bottom temperature anomalies of > 10 °C (Fig. 2c). During the initial 1–2 days of this storm, the winds created an energetic cross-shelf circulation of speeds of 0.2–0.4 m/s (Fig. 2b). Despite unchanged wind conditions, this circulation and the preexisting ambient density stratification then suddenly collapsed and largely disappeared on a timescale of ~ 12 h. Lentz (2001) interpreted the observed shutdown of the cross-shelf circulation as the consequence of an unstratified water column which, according to Lentz (2001), increased the thickness of the surface and bottom Ekman layers such that their interference canceled out any cross-shelf flow.

For completeness, it should be added that the cross-shelf circulation in the shallower nearshore zone (< 5 m water depth) follows from the effects of wave breaking and other nonlinear wave effects (e.g., Greenwood and Osborne 1990), leading to the creation of rip currents and undertows. On shorter timescales of hours, offshore or onshore wind bursts can also induce cross-shelf circulations in shallow water (< 10 m deep). Offshore wind bursts lead to shallow upwelling circulations, known as lee effect (e.g., Hela 1976), in which the transverse currents enhance the static stability in shallow water which lowers turbulence levels (Kämpf 2015). On the other hand, the downwelling circulation driven by onshore wind bursts can trigger enhanced vertical mixing due to shear-flow instabilities (Kämpf 2017). While the circulation induced by cross-shelf winds can be an important transport agent for larvae (e.g., Tilburg 2003), its vertical reach is generally limited to shallow water (< 10 m), except for shelf seas

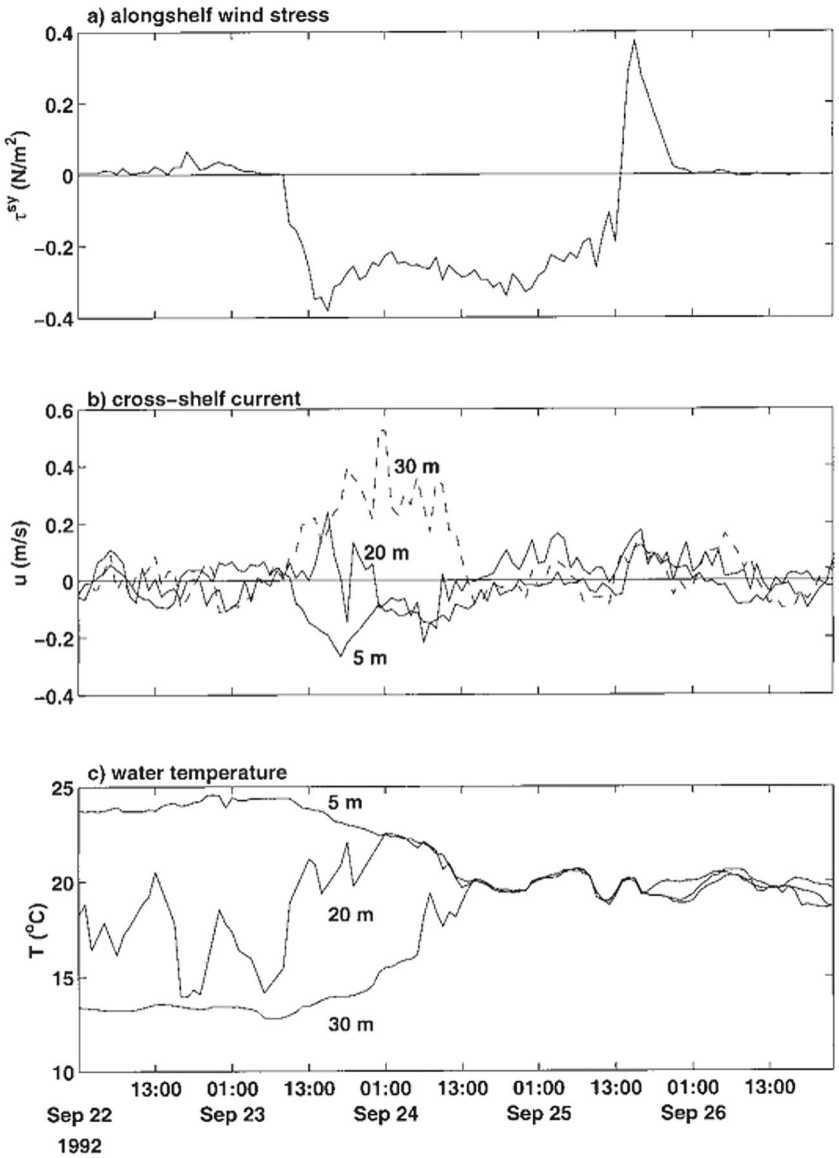

Fig. 2 Time series (22–27 September 1992) of **a** along-shelf wind stress (Pa), **b** cross-shelf current velocity (m/s), and **c** sea-water temperature (°C) at a coastal mooring station over the North Carolina Shelf at water depth of ~ 35 m. **b**, **c** Data from 5 m, 20 m, and 30 m of the water column. Taken from Lentz (2001)

at low latitudes such as the Arafura Sea, where this can exceed 50 m (see Kämpf 2015).

Sediment erosion follows once the shear stress near the seabed exceeds a certain threshold value. It is common knowledge that this value depends strongly on seafloor properties (sediment type and grain-size distribution, organic matter content). Apart from the effect of breaking waves in the surf zone, there are different causes of sediment erosion in shelf seas. North Sea studies, for instance, reveal that under normal and moderate weather conditions, tidal currents are most effective in eroding sediments locally in regions of strong tidal flows such as tidal inlets (Lettmann et al. 2009). During strong winds and storm-surge conditions, on the other hand, surface gravity waves (wind waves and swell) have a dominant effect on suspended particle dynamics in shallower shelf regions, in particular in narrow straits and inlets (Stanev et al. 2009; Schloen et al. 2017). The effects of tides and waves on bed shear stress are ignored in this work.

As a guide, the erosion of sand-mud mixtures can be initiated above critical bed shear stresses of ~ 0.1–0.2 Pa (Mitchener et al. 1996). In the context, let us revisit observations from the US middle Atlantic continental shelf (mid-MAB). For instance, using near-bed current data from tripod deployments and wave spectra from National Data Buoy Center (NDBC) buoy 44008, Chang et al. (2001) estimated the bottom stress at locations in and near the Mud Patch (silt plus clay content over 30% at study sites) during the fall of 1996 for comparisons with beam attenuation data. They

determined that the passage of hurricanes Edouard and Hortense resulted in combined wave–current stresses in excess of 0.35 Pa at a depth of 70 m, and resuspension occurred at a critical stress of 0.08 Pa. Churchill et al. (1994) estimated bottom stress at four sand-dominated (silt plus clay content of 1.1–1.6%) locations located across shelf in the mid-MAB at depths ranging from 40 to 130 m, and determined the critical stress threshold for resuspension varied between 0.08 and 0.22 Pa. On the basis of this observational evidence, bed shear stresses > 0.35 Pa outside the littoral zone are hereafter referred to as "extreme."

Motivated by earlier studies (de Szoeke and Richman 1984; Allen et al. 1995; Allen and Newberger 1996; Lentz 2001; Austin and Lentz 2002; Wijesekera et al. 2003; Kirincich et al. 2005), this work employs a 2.5-dimensional hydrodynamic shelf model to revisit the dynamics of the wind-driven circulation in coastal oceans. In contrast to previous investigations, this work focusses on resultant bed-shear stresses, a feature that has not received much attention before.

2 Materials and methods

2.1 Model description

2.1.1 Overview

This study applies a z-coordinate hydrodynamic shelf model with a free sea surface developed by Kämpf (2010). The model is used here as a shelf model with a relatively coarse horizontal grid spacing of $\Delta x = 1$ km and a vertical grid spacing of $\Delta z = 1$ m, noting that this setting filters away nonhydrostatic instability processes (Kämpf 2010). In contrast to sigma coordinates, the use of a Cartesian vertical coordinate leads to a stepwise representation of sloping terrains. This did not cause any significant biases in this study. Sub-grid scale mixing is parameterized by a standard k-ε turbulence closure scheme (Rodi 1987; Burchard et al. 1998). Except for one experiment considering upwelling-favorable wind forcing, all experiments discussed in this work are driven by downwelling-favorable coastal winds. Sensitivity studies consider variations of obvious parameters that are expected to influence either directly or indirectly bed-shear stresses such as the wind-stress magnitude, the bottom drag coefficient, and the structure of the seawater density field.

Appendix A presents results of simulations of the modified shelf model in which the k-ε turbulence scheme is replaced by a modified Kochergin's turbulence closure (Kochergin 1987). The aim of this supplementary study is to explicitly reveal that the shear-flow instability mechanism is the leading source of the creation of extreme bed shear stresses. In addition, Appendix B presents an approach in which predictions from the shelf model are used to initialize a high-resolution model version, similar to the "super-parameterization" approach used by Campin et al. (2011) in their study of open-ocean deep convection. Here, the high-resolution model version employs a finer grid spacing ($\Delta x = \Delta z = 1$ m) which allows for the direct numerical simulation of nonhydrostatic stirring processes (see Kämpf 2010). The aim of this approach is to test whether the resolved shear-flow instabilities are the trigger of enhanced bed shear stresses.

2.1.2 Model domain and initial density stratification

The model domain used in this work consists of a simplified continental shelf in which the total water depth, h, changes according to (Fig. 3):

$$h(x)/h_\infty = \min\left\{\left[0.1 + 0.3(x/x_o)^{0.25}\right], 1\right\} \quad (1)$$

where $x_o = 1$ m is a dummy parameter, and the maximum total water depth is taken as $h_\infty = 100$ m. This nonlinear shape, which is taken as characteristic of many coastal oceans, implies that total water depth increases sharply from the coast to ~ 60 m within a distance of ~ 10 km, before entering a regime of milder bottom slopes. The specific shape of the seafloor chosen has no significant impact on the general results presented in this work.

Initially, the water body consists of a weakly stably stratified surface layer, 50 m in thickness, characterized by a stability frequency of $N^2 = 3.82 \times 10^{-4}$ s^{-2} (calculated from $N^2 = -g/\rho_o \partial\rho/\partial z$, where $g = 9.81$ m/s^2 is acceleration due to gravity, ρ is seawater density of a typical average value of $\rho_o = 1026$ kg/m^3, and z is the vertical coordinate). A pronounced pycnocline with a sharp density change over a vertical distance of 5 m separates the surface layer from a bottom layer, which is also weakly stably stratified ($N^2 = 3.82 \times 10^{-4}$ s^{-2}). The pycnocline itself has a strong stabilizing stability frequency of $N^2 = 3.8 \times 10^{-3}$ s^{-2}, which corresponds to a minimum internal wave period of ~ 100 s. The Coriolis parameter is set to $f = +1 \times 10^{-4}$ s^{-1} representing mid-latitudes of the northern hemisphere. Note that this yields an internal deformation radius of 6–10 km at distances > 20 km from the shore for the density configuration used. The density structure (i.e., static stabilities of surface layer and pycnocline; vertical position of pycnocline) is varied in sensitivity experiments.

2.1.3 Model equations

Using the Boussinesq approximation and the assumption that there are no gradients of variables in the alongshore direction, the momentum equations can be written as:

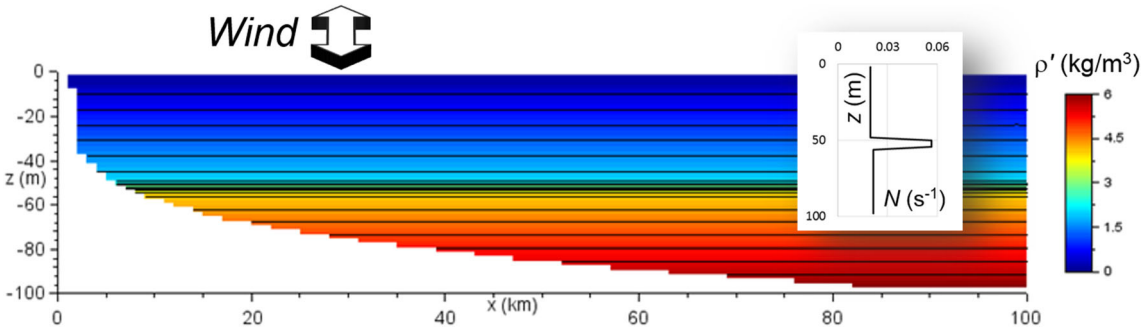

Fig. 3 Shelf model domain and initial density stratification (color shading, and contours) used in all wind-forcing scenarios. The insert displays the vertical distribution of stability frequency, N

$$\frac{\partial}{\partial t}u + u\frac{\partial}{\partial x}u + w\frac{\partial}{\partial z}u - fv = -\frac{1}{\rho_o}\frac{\partial}{\partial x}P + \frac{\partial}{\partial x}\left(A_x\frac{\partial}{\partial x}u\right) + \frac{\partial}{\partial z}\left(A_z\frac{\partial}{\partial z}u\right) \quad (2)$$

$$\frac{\partial}{\partial t}v + u\frac{\partial}{\partial x}v + w\frac{\partial}{\partial z}v + fu = \frac{\partial}{\partial x}\left(A_x\frac{\partial}{\partial x}v\right) + \frac{\partial}{\partial z}\left(A_z\frac{\partial}{\partial z}v\right) \quad (3)$$

$$\frac{\partial}{\partial t}w + u\frac{\partial}{\partial x}w + w\frac{\partial}{\partial z}w = -\frac{1}{\rho_o}\frac{\partial}{\partial z}P - \frac{\rho'}{\rho_o}g + \frac{\partial}{\partial x} \times \left(A_x\frac{\partial}{\partial x}w\right) + \frac{\partial}{\partial z} \times \left(A_z\frac{\partial}{\partial z}w\right) \quad (4)$$

where t is time; x and z are Cartesian coordinates (z pointing upwards); u, v, and w are velocity components; f is the Coriolis parameter; P is dynamic pressure; ρ′ is density anomaly; and A_x and A_z are horizontal and vertical eddy viscosities. For simplicity, a constant value of $A_x = 4$ m^2/s is assumed, as also used by Wijesekera et al. (2003). Wind forcing is implemented via the surface boundary condition:

$$A_z\partial u/\partial z = 0 \quad \text{and} \quad A_z\partial v/\partial z = \tau_y/\rho_o \quad \text{for z} = 0 \quad (5)$$

where τ_y is a prescribed alongshore wind-stress component. A quadratic friction law with a friction parameter of $r = 0.002$ is applied to horizontal flows in the bottom-nearest grid cells.

$$A_z\partial u/\partial z = ru\sqrt{u^2+v^2} \text{ and } A_z\partial v/\partial z = rv\sqrt{u^2+v^2} \text{ for } z = -h \quad (6)$$

The value of r is varied in sensitivity experiments. Note that $r = 0.002$ in conjunction with a vertical grid spacing of 1 m is equivalent to a bed roughness height of $K_s \approx 2$ mm. This can be derived from the law of the wall, which implies that $\sqrt{r} = \kappa/\ln(30\ell/K_s)$, where $\kappa = 0.4$ is the von Kármán constant, $\ell = \Delta z/2 = 0.5$ m is the distance of the bottom-nearest velocity grid point from the seafloor.

There are no flow across impermeable surfaces and $w = 0$ in the uppermost model layer. Zero-slip lateral boundary conditions are used for the along-slope velocity component v to eliminate biases that could otherwise develop at horizontal surfaces of the step-like bathymetry in z-coordinates.

Under the assumption of a linear equation of state, the evolution of density anomalies can be predicted from the advection-diffusion equation:

$$\frac{\partial}{\partial t}\rho' + u\frac{\partial}{\partial x}\rho' + w\frac{\partial}{\partial z}\rho' = \frac{\partial}{\partial x}\left(K_x\frac{\partial}{\partial x}\rho'\right) + \frac{\partial}{\partial z} \times \left(K_z\frac{\partial}{\partial z}\rho'\right) \quad (7)$$

where horizontal eddy diffusivity is taken the same as horizontal eddy viscosity ($K_x = A_x$). A turbulent Prandt number of $Pr = 0.7$ is assumed to compute vertical eddy diffusivity, i.e., $K_z = A_z/Pr$. Variations of Pr did not significantly change the results. There are no density fluxes across impermeable surfaces including the sea surface.

Volume conservation has two forms in the model. One form is the continuity equation, being valid for any volume element within the model domain, which is given by:

$$\frac{\partial}{\partial x}u + \frac{\partial}{\partial z}w = 0 \quad (8)$$

On the other hand, vertical integration of Eq. (8) over the entire water column gives a prognostic equation for pressure due to sea surface elevation, P_s. This equation can be written as:

$$\frac{\partial}{\partial t}P_s = \rho_o g\frac{\partial}{\partial x}\left(\int u\,dz\right) \quad (9)$$

Note that Eq. (9) continuously updates the boundary pressure values in Eqs. (2) and (3) after each iteration step of the simulation. Sea surface elevation can be diagnosed from the hydrostatic relation $\eta = P_s/(\rho_o g)$. Zero-gradient conditions are used for all variables at the open-ocean boundary, except for

sea-level elevation which is kept at zero during the simulation, i.e., $P_s = 0$.

The dynamic pressure field (which accounts for effects of the free sea surface) is iteratively derived from a successive over-relaxation (SOR) scheme (see Kämpf 2010). To minimize numerical diffusion, advection is computed using a total variance diminishing (TVD) scheme with a superbee limiter (see Kämpf 2009).

The numerical time step is set to $\Delta t = 2$ s, constrained by the CFL stability condition associated with the propagation speed of barotropic surface gravity waves. The total simulation time of experiments is 10 days which corresponds to the upper timescale bound of synoptic weather events. To avoid initial disturbances in the form of unwanted inertial oscillations or gravity waves, the wind-stress field, assumed spatially uniform, is temporally adjusted from zero to its final value in a range of 0.1–0.2 Pa (corresponding to wind speeds of 9–12 m/s) over the first 2 days of simulations.

2.1.4 Turbulence closure

Vertical eddy viscosity, A_z, is predicted from a k-ε turbulence model as the product of a turbulent length scale with a turbulent velocity scale (e.g., Kuzmin et al. 2007), that is:

$$A_z = \max\left[l_*\sqrt{k}, \nu_{\min}\right] \tag{10}$$

where l_* is a turbulent mixing length, k is the kinetic energy of turbulent velocity fluctuations, and $\nu_{\min} = 10^{-6}$ m^2 s^{-1} is the molecular value. The turbulent mixing length is given by:

$$l_* = \min\left(c_\mu k^{3/2}/\varepsilon, l_{\max}\right) \tag{11}$$

where $c_\mu = 0.09$ is an empirical constant, ε is dissipation of turbulent kinetic energy, and $l_{\max}$ is an upper bound of l_*, being defined as distance from either the seafloor or the sea surface, whichever is smaller. The parameter $l_{\max}$ is a bound for the size of the largest vortices. Turbulent kinetic energy, k, and dissipation rate, ε, are estimated by their balance equations:

$$\frac{\partial}{\partial t}k + u\frac{\partial}{\partial x}k + w\frac{\partial}{\partial z}k = \frac{\partial}{\partial x}\left(A_h\frac{\partial}{\partial x}k\right) + \frac{\partial}{\partial z} \times \left(\nu_k\frac{\partial}{\partial z}k\right) + P_k - S_b - \varepsilon \tag{12}$$

$$\frac{\partial}{\partial t}\varepsilon + u\frac{\partial}{\partial x}\varepsilon + w\frac{\partial}{\partial z}\varepsilon = \frac{\partial}{\partial x}\left(A_h\frac{\partial}{\partial x}\varepsilon\right) + \frac{\partial}{\partial z}\left(\nu_\varepsilon\frac{\partial}{\partial z}\varepsilon\right) + \frac{\varepsilon}{k}\left(c_{\varepsilon 1}P_k - c_{\varepsilon 3}S_b - c_{\varepsilon 2}\varepsilon\right) \tag{13}$$

where the diffusion parameters are given by $\nu_k = A_z/\sigma_k$ and $\nu_\varepsilon = A_z/\sigma_\varepsilon$ (with the standard settings of $\sigma_k = 1.0$ and $\sigma_\varepsilon = 1.3$), P_k denotes the production term, and the S_b term represents the effects of density stratification. Turbulence production and stratification effects can be expressed as:

$$P_k = A_z\left[(\partial u/\partial z)^2 + (\partial v/\partial z)^2\right] \tag{14}$$

$$S_b = -A_z/\rho_o g\partial\rho'/\partial z \tag{15}$$

The numerical parameters in Eqs. (12) and (13) are set to their standard values ($c_{\varepsilon 1} = 1.44$, $c_{\varepsilon 2} = 1.92$, $c_{\varepsilon 3} = 0.4$ for stable stratification, $c_{\varepsilon 3} = -1$ for unstable stratification). Zero-gradient conditions are used for both k and ε at all horizontal boundaries. Zero-gradient conditions are used for k at both the surface and bottom of the water column. The boundary condition for ε at both the sea surface and the seafloor can be written as:

$$\varepsilon|_{\text{sea floor}} = c_\mu|u_*|^{3/2}\kappa^{-1}(\ell + z_o)^{-1} \tag{16}$$

where the bed roughness length is given by $z_o = K_s/30$. At the sea surface, the magnitude of the friction velocity in Eq. (16) is given by:

$$|u_*| = \sqrt{\tau_x^2 + \tau_x^2}/\rho_o \tag{17}$$

At the seafloor, the friction velocity in Eq. (16) is calculated from the near-bottom horizontal velocity components via:

$$|u_*| = \sqrt{r(u^2 + v^2)} \tag{18}$$

2.1.5 Description of experiments

Most experiments of this work (Table 1) are run with a wind-stress magnitude of 0.2 Pa, corresponding to a wind speed of ~ 11 m/s at a reference height of 10 m above sea level. The prescribed wind field is upwelling-favorable in experiment U-1 ("U" for upwelling), but downwelling-favorable in the control simulation of experiment D-1 ("D" for downwelling) and all other numerical experiments.

The initial pycnocline is shifted upward to a depth of 25 m in experiment D-2, but downward to a depth of 70-m in experiment D-3 (without changing the static stabilities inside the surface and bottom layers). In experiment D-4, the static stability of the upper layer of the water column is increased fivefold relative to the control setting to $N^2 = 1.91 \times 10^{-3}$ s^{-2} without changing the static stabilities of the pycnocline and the bottom layer.

Experiment D-5 considers a doubling of the friction parameter to $r = 0.004$, which corresponds to a tenfold increase of the bed roughness parameter in (16) to 2 cm. Experiments DRW-1 and DRW-2 are repeats of experiments D-1 and D-4, but with half the wind-stress magnitude of 0.1 Pa.

Table 1 List of experiments

Experiment ID	Description
U-1	$\tau_y = +0.2$ Pa; upwelling-favorable winds
D-1*	$\tau_y = -0.2$ Pa; downwelling-favorable winds
D-2	$\tau_y = -0.2$ Pa; shoaling of initial pycnocline to 25 m
D-3	$\tau_y = -0.2$ Pa; deepening of initial pycnocline to 70 m
D-4	$\tau_y = -0.2$ Pa; fivefold increase in upper-ocean static stability
D-5	$\tau_y = -0.2$ Pa; $r = 0.004$; tenfold increase of roughness length
DRW-1	$\tau_y = -0.1$ Pa; 50% reduced wind stress
DRW-2	$\tau_y = -0.1$ Pa; fivefold increase in upper-ocean static stability

*Control experiment

3 Results and discussion

3.1 Upwelling-favorable wind forcing

Upwelling-favorable wind leads to the development of full upwelling (i.e., sub-pycnocline water reaching the sea surface) within 5 days of simulation (Fig. 4a). Hereby the wind forcing induces offshore water transport in the surface Ekman layer. The resultant flow divergence lowers the coastal sea level, which creates a geostrophic along-shelf geostrophic flow with onshore transport of water in the bottom Ekman layer. Despite some weakening in shallower water, both the surface and the bottom Ekman layer extent close to the shore (Fig. 4b), in agreement with previous studies (e.g., Allen et al. 1995). The resultant Ekman layers have a thickness of 10–20 m; and associated cross-shelf currents attain speeds of 0.1–0.2 m/s.

The barotropic pressure gradient due to the sloping sea surface supports the development of a swift (> 1 m/s near the surface) geostrophic upwelling jet (Fig. 4c). Due to strong density stratification in near-bottom water, reinforced by the onshore flow of denser water in the bottom Ekman layer, the upwelling jet remains detached from the seafloor. Note that the baroclinic component of the jet is confined to the baroclinic radius of deformation (~ 7–10 km for the model configuration used), whereas the barotropic component extends to the open ocean and allows for the establishment of a bottom Ekman layer far offshore. Turbulent levels remain relatively low due to stratification effects in most of the simulated coastal ocean (Fig. 4d). Some moderate enhancement

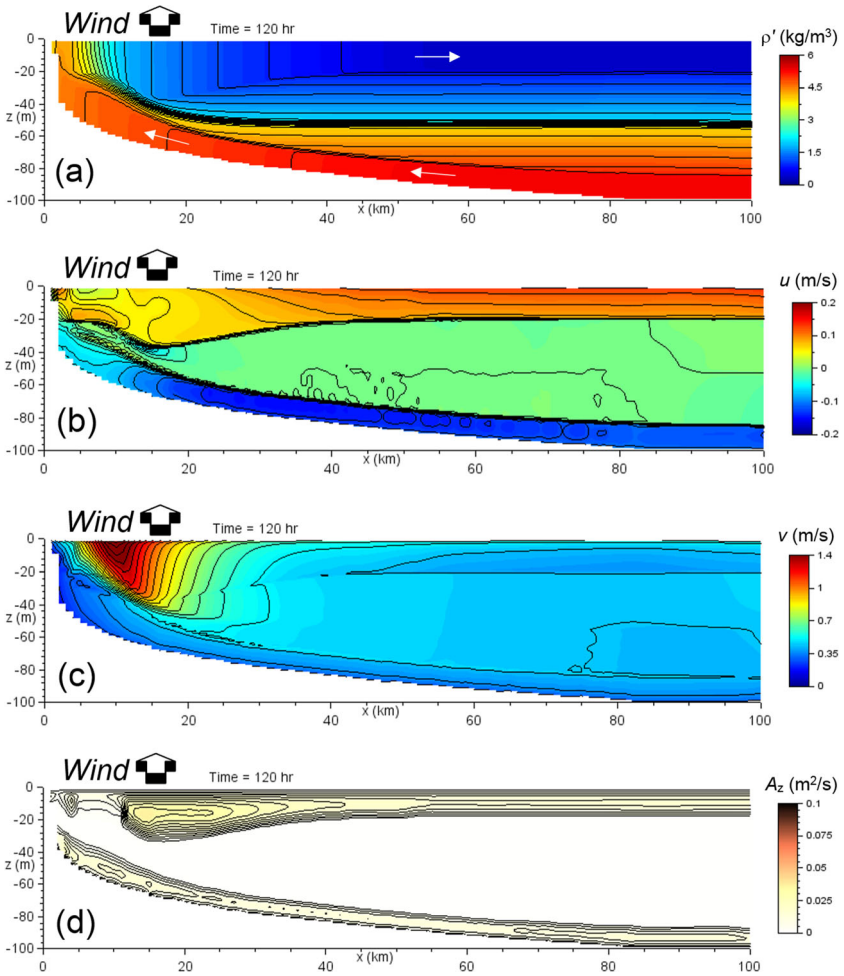

Fig. 4 Experiment U-1. Distributions (color shading) after 5 days of simulation of **a** density excess ρ′ (kg/m^3), **b** cross-shelf velocity component u (m/s), **c** along-shelf velocity component v (m/s), and **d** vertical eddy viscosity A_z (m^2/s). Arrows (**a**) indicate cross-shelf flow directions in Ekman layers. Lines are contours (CI arbitrary)

of turbulence levels is seen in the frictional boundary layers with values of $A_z \sim 0.02$ m^2/s. Overall, the simulation results for experiment U-1 agree well with previous model predictions by Wijesekera et al. (2003).

Farther offshore and outside the upwelling zone, flow in the bottom Ekman layer creates moderate bed shear stresses of ~ 0.2 Pa (Fig. 5). Initially, bed-shear stresses are markedly reduced in near-shore water due to density stratification effects. Over time, bed shear stresses in shallower water tend to increase on a time scale of ~ 5 days that reach the offshore value of ~ 0.2 Pa. Hence, we can conclude that, apart from Ekman-layer effects that may cause marginal sediment erosion in offshore waters, coastal upwelling events are not expected to create extreme bed shear stresses unless there are other additional processes at work (e.g., strong tidal currents).

3.2 Downwelling-favorable wind forcing (control experiment)

In contrast to the upwelling scenario, a reversal of coastal winds creates onshore flow in the surface Ekman layer. This onshore flow pushes surface water against the shore from where it returns in an undercurrent (Fig. 6a). The shear flow instability that follows from this shear flow in conjunction with convective instabilities leads to the development of vigorous turbulent mixing in nearshore waters. Associated vertical eddy viscosities and diffusivities ($A_z \sim 0.1$ m^2/s) are fivefold larger than in the upwelling case (Fig. 6d, see Fig. 4d). The associated Ekman layer thickness, $(2A_z/f)^{1/2}$, increases to ~ 45 m, resulting in a substantial interference between surface and bottom Ekman layers in shallower water (e.g., Kämpf 2015; Lentz 2001). The associated intensified vertical mixing homogenizes not only the density field near the shore (see Fig. 6a), but also the cross-shelf velocity component u (Fig. 6b). Accordingly, the cross-shelf circulation weakens substantially and "shuts down" in this mixing region, in agreement with previous studies (e.g., Allen and Newberger 1996). It should be noted that the shutdown of the cross-shelf circulation described here cannot be understood from the analytical theories used by McCreary and Kundu (1985) and Fennel (1999) and related works, as these perturbation theories did not consider mixing effects.

Note that, farther offshore, the offshore movement of relatively lighter fluid by the near-bottom flow induces convective

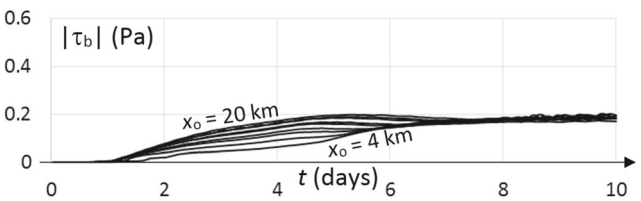

Fig. 5 Experiment U-1. Time series of the magnitude of bed shear stress (Pa) in the region as a function of offshore distance from $x_o = 4$ to 20 km shown at an interval of 2 km

stirring in the bottom Ekman layer (which is parameterized in the shelf model). Moum et al. (2004) explicitly analyzed such bottom Ekman layer effects during downwelling.

The barotropic pressure gradient due to the sloping sea surface supports the establishment of a downwelling coastal jet that is centered here over the transition zone between unstratified and stratified waters (Fig. 6c). The surface flow attains speeds of ~ 1 m/s. This frontal current coincided with a marked sub-surface density front that establishes in near-bottom waters. Importantly and in stark contrast to the upwelling case, the along-shelf current of the frontal flow become influenced by the enhanced vertical momentum diffusion developing in the near-shore mixing zone. This effect intensifies the near-bottom flow.

In the following, the evolution of the simulated density and velocity fields are compared for a fixed offshore distance at $x_o = 10$ km, where the model's total water depth is ~ 60 m, with the mooring data over the North Carolina Shelf (see Fig. 2). At the selected location, the near-bottom density starts to gradually decrease under the effects of advection and diffusion after 2 days of simulation (Fig. 7a). Top-to-bottom density differences have disappeared by the 4th day of simulation. During the initial 4 days, the cross-shelf circulation attains speeds of 0.1–0.2 m/s (Fig. 7b) while the along-shelf surface current strengthens to speeds > 1 m/s (Fig. 7c).

Around the time of density homogenization, the cross-shelf circulation weakens significantly within a time scale of ~ 12 h. This delay of the weakening of the cross-shelf circulation relative to the start of the wind event and the built-up of a noticeable cross-shelf circulation before its "shutdown" is in principal agreement with observational evidence (see Fig. 2). During this transition, the near-bottom along-shore velocity component intensifies from ~ 0.29 to ~ 0.45 m/s before relaxing back to ~ 0.31 m/s. This transient intensification of v that triggers a transient extreme bed shear stress > 0.4 Pa (Fig. 8). The resultant bed shear stress during coastal downwelling is substantially larger than that induced by coastal upwelling (see Fig. 5).

In the shelf model, the sudden enhancement of turbulence levels in nearshore water is the consequence of shear-flow instabilities, also known as Kelvin-Helmholtz (KH) instability (Drazin and Reid 1981; Baines and Mitsudera 1994). One necessary condition for this instability is that the gradient Richardson number; that is,

$$Ri_g = N^2 / \left[(\partial u/\partial z)^2 + (\partial v/\partial z)^2 \right] \tag{19}$$

which is the ratio between Eqs. (15) and (14), falls below a threshold value of ¼ at some level in the flow. In addition, the horizontal velocity field has to have an inflection point, which is satisfied for any cross-shelf circulation (Kämpf 2017). It is obvious that the gradual decrease in the top-to-bottom density difference (while the vertical shear of the horizontal velocity components remains largely unaffected), as shown in Fig. 7, leads to a gradual decrease of Ri_g. In fact, at $x_o = 10$ km, the

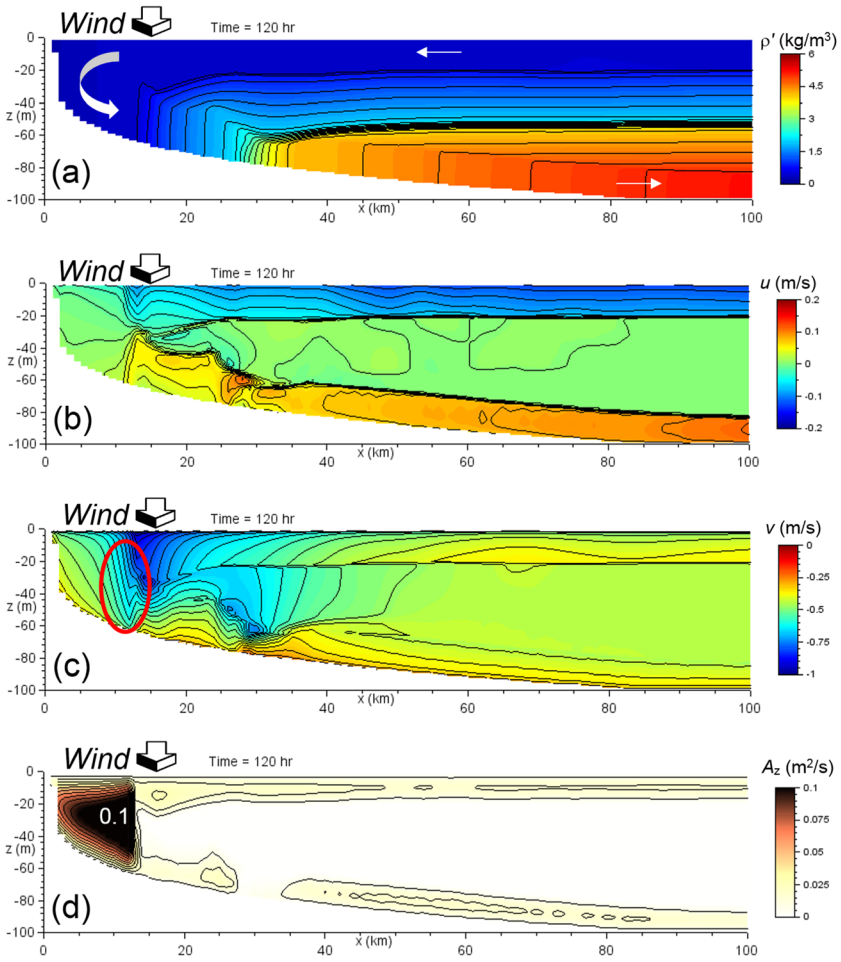

Fig. 6 Same as Fig. 4, but for experiment D-1. The ellipse (**c**) highlights a region of enhanced along-shelf momentum, *v*, near the seafloor

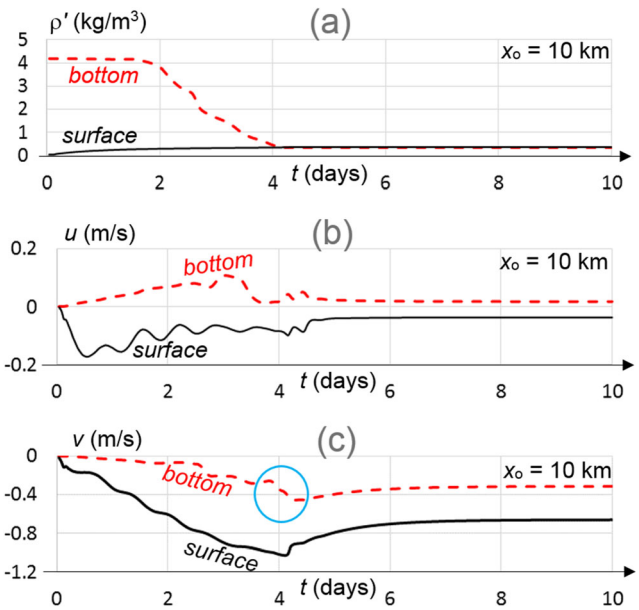

Fig. 7 Experiment D-1. Time series of **a** density anomalies, ρ' (kg/m^3), **b** cross-shelf velocity component, u (m/s) and **c** along-shelf velocity component, v (m/s), near the surface and bottom of the water column at an offshore distance of $x_o = 10$ km. The ellipse (**c**) highlights a transient enhancement of v near the seafloor

gradient Richardson number approaches a zero value after ~ 3.5 days of simulation (Fig. 9). Note that the vertical shear of v rather than u (see Fig. 7b, c) is dominant in the denominator of Eq. (19).

Additional simulations in which the Ri_g effect is explicitly formulated in the turbulence closure (see Appendix A) and high-resolution direct nonhydrostatic simulations (see Appendix B) confirm the leading role that KH instabilities play in the dynamics described here.

Indeed, the shelf model cannot directly simulate nonhydrostatic mixing processes. Hence, the weakening of the cross-shelf circulation in the shelf model is exclusively related to the increase in eddy viscosity and the associated

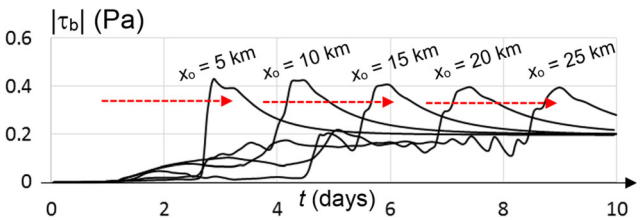

Fig. 8 Experiment D-1. Time series of the magnitude of bed shear stress, τ_b (Pa), at selected offshore locations, x_o

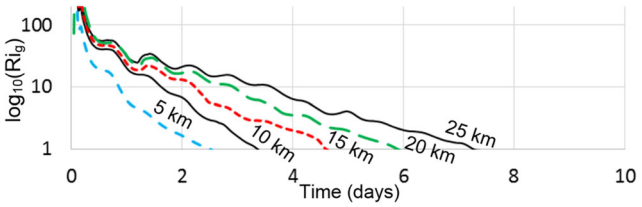

Fig. 9 Experiment D-1. Time series of the gradient Richardson number, expressed as $\log_{10}(Ri_g)$, calculated from Eq. (19) using top-to-bottom differences of density and velocity shear. Small values of $Ri_g < ¼$ are reached first in nearshore water and then progressively later farther offshore. The fluctuations seen are inertial oscillations of a period ($T = 2\pi/f$) of ~ 17.5 h

increase in the thickness of Ekman layers. This leads to an interference of surface and bottom Ekman layers and a weakening of the cross-shelf circulation (Kämpf 2015), which is consistent with the interpretation by Lentz (2001).

Enhanced turbulence levels due to KH instabilities affect both the density field (Fig. 10a) and the momentum distributions on the time scale of the initial mixing process (~ hours). In turn, a modified static stability also influences the thickness of Ekman layers on rotational time scales (~ days). Given that the cross-shelf circulation has a vanishing vertical average, it is clear that enhanced vertical diffusion/mixing of momentum leads to a weakening of the cross-shelf circulation (Fig. 10b). This overall change of the cross-shelf circulation is accompanied by a complex transition of the cross-shelf flow component that develops a transient peak at an intermediate depth of 33–40 m after 4 days of simulation.

Unlike the cross-shelf flow component, the vertical profile of the along-shelf flow component v does not change sign and, therefore, has a non-zero vertical average. Given that v decreases with depth, the sudden enhancement of vertical diffusion therefore leads to an intensification of v near the seabed around day 4 of the simulation (Fig. 10c). After this relatively rapid mixing episode, which takes place on a sub-rotational timescale (< 1 day), the Ekman layer dynamics re-adjusts to the change in turbulent viscosity, which leads to a subsequent reduction of the bed shear stress.

Another important feature revealed here is that the zone of peak bed shear stresses develops first within a few kilometers from the coast and then gradually moves farther offshore (see Fig. 8). This offshore movement is aligned with the offshore progression of the downwelling front which involves the "opening" of new terrain for the development of shear-flow instabilities (see Fig. 8 and Appendix B). In the control experiment, the speed of this offshore progression of the zone of maximum bed shear stresses is ~ 3 km per day. The total offshore distance affected by this process—which operates like a seabed "plow"—depends on different factors (see case studies), but most importantly on the magnitude of downwelling-favorable wind stress and the duration of a synoptic wind event. For instance, a wind event of 4 days of duration with a wind-stress magnitude of 0.2 Pa (as in the control experiment) will cover an offshore distance of ~ 8–9 km, whereas a prolonged event of 8 days induration will cover an offshore distance of ~ 22 km (see Fig. 9).

3.3 Case studies

In the control experiment D-1, the bed shear stress peaks at a value of ~ 0.4 Pa at the location $x_o = 10$ km after ~4.5 days of simulation. In the following, these values are used as a time-scale T and as a scale of the intensity τ^* of the maximum bed

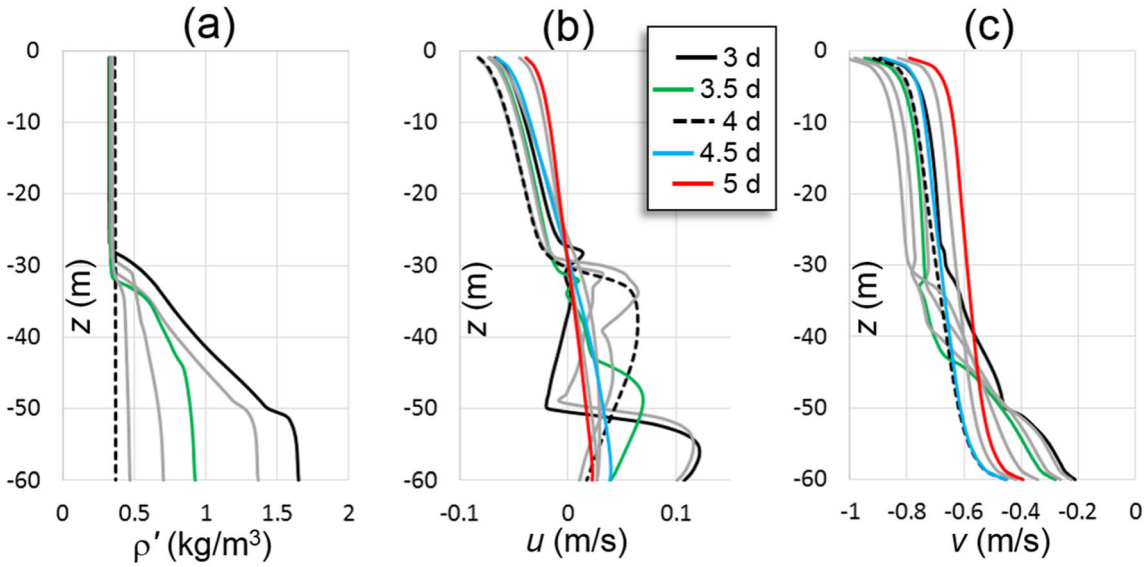

Fig. 10 Experiment D-1. Evolution of vertical profiles of **a** density anomaly ρ' (kg/m^3), **b** cross-shelf velocity component u (m/s), and **c** along-shelf velocity component, v (m/s), at $x_o = 10$ km from days 3 to 5 of the simulation shown every 6 h and color-coded every 12 h. The density profile remains well mixed from the 4th day of simulation onwards

shear stress for comparisons with the findings of other case studies (see Table 1).

A variation of the vertical location of the pycnocline (experiments D-2 and D-3) only slightly modifies the timescale *T*. For a shallower pycnocline there is a slight delay of *T* by 0.4 days (Fig. 11a), whereas a deeper pycnocline triggers an earlier appearance of the bed shear stress maximum by a few hours (Fig. 11b). Surprisingly, the initial depth of the pycnocline has a strong effect on the intensity of bed shear stresses. In particular, a shallower pycnocline (shifted from 50 to 25 m in experiment D-2) leads to a 50% increase in τ^* to a value of ~ 0.6 Pa (Fig. 11a). In contrast, deepening of the initial pycnocline from 50 to 70 m only marginally reduces τ^* to a value slightly below 0.4 Pa (Fig. 11b).

Experiment D-4 considers a much stronger stratified surface layer (see Table 1) to further test the effect that the upper-ocean density stratification has on the resultant τ^*. The density in the upper 50 m of the water column varies initially linearly by 10 kg/m^3. This density change corresponds to an (unrealistic) vertical temperature gradient of ~ 40 °C for an isohaline layer or a (more realistic) vertical salinity gradient of 10 units for an isothermal layer. In this situation, the value of τ^* dramatically increases to > 1 Pa, but the offshore movement of the frontal zone slows down (Fig. 11c). Now, it takes about 7 days for the zone of peak shear stresses to reach an offshore distance of 10 km. The increase in bed shear stresses in experiment D-4 is again directly affiliated with the downward diffusion/mixing of the along-shelf frontal current (Fig. 12).

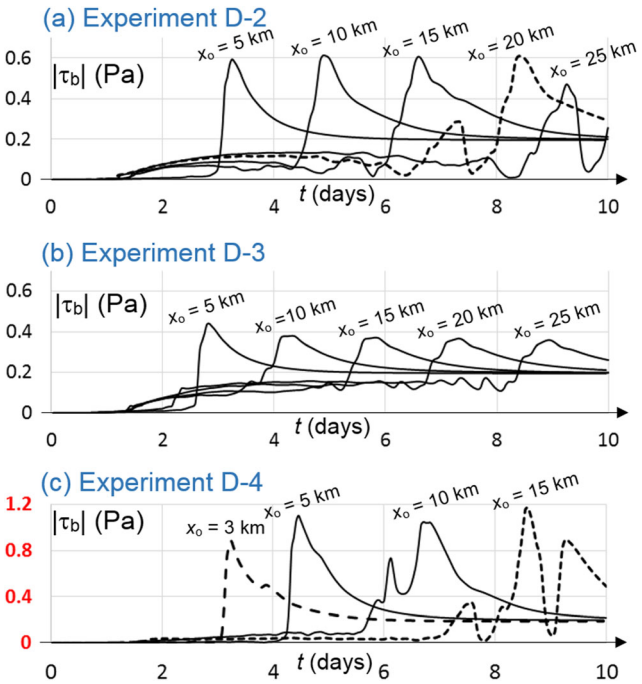

Fig. 11 Same as Fig. 9, but for different case studies (see Table 1). The *y*-axis of **c** is shown in red to highlight the extremely high bed shear stresses (> 1 Pa) that develop in experiment D-4

A tenfold increase of the bed roughness from 2 mm to 2 cm in experiment D-5 only leads to a ~ 25% increase in τ^* and a slight decrease in the offshore progression speed of the downwelling front (Fig. 13a, compared with Fig. 9). This relatively weak enhancement of τ^* is due a friction-related weakening of the near-bottom flow which partially compensates the greater bed roughness in the resultant bed shear stress.

On the other hand, a decrease of the wind-stress magnitude from 0.2 to 0.1 Pa (experiment DRW-1) leads to a marked decrease in the offshore progression speed from 3 to 1 km/day (Fig. 13b, compared with Fig. 9). Accordingly, the width of impact zone decreases to 5 km on a synoptic timescale of 5 days. τ^* reduces to a value of 0.3 Pa. A reduced wind stress of 0.1 Pa in combination with enhanced upper-ocean density stratification (experiment DRW-2) leads to establishment of a zone of extreme bed shear stresses > 0.4 Pa (Fig. 13c). On a timescale of 5 days, this impact zone would extend ~ 2.5 km offshore.

3.4 Ecological implications

Coastal oceans are generally much more biologically productive than the open ocean (Kämpf and Chapman 2016). Two key processes underpinning this high productivity are nutrient discharges via continental runoff and the upwelling of nutrient-rich seawater from the open ocean. From ample observations, it turns out that large fraction of the total productivity in coastal oceans is fueled by recycled nutrients either via bacterial regeneration at the sediment-water interface and in the water column, or by grazing activities of herbivores.

The supply of nitrogen as dissolved nitrate can be differentiated as "new" production fueled by nitrate and "regenerated" production fueled by recycled ammonium and urea. This fraction is conventionally expressed by the *f* ratio—the ratio between new and regenerated production (Eppley and Peterson 1979).

The *f* ratio varies between 0.1 in the open ocean and other oligotrophic regions and up to 0.8 in some coastal upwelling regions (Laws 2004). In particular, benthic recycling in the form of ammonification may account for 20–80% of the nitrogen requirements of phytoplankton in shallow water (< 50 m) ecosystems (Nixon 1981; Jensen et al. 1990; Hansen and Blackburn 1992). While some nutrient recycling takes place on short timescales within the water column, substantial fractions of regenerated nutrients enter the water column via the resuspension of seabed sediment (e.g., Fanning et al. 1982; Herbert 1999). Downwelling-induced extreme bed shear stresses, identified here, may contribute to the observed high levels of regenerated production in coastal oceans.

Findings of this and previous studies indicate that, before its shutdown, the cross-shelf circulation can still displace passive particles such as larvae over vast horizontal distances of ~ 20–50 km. Such a delay would explain the observed onshore larval transport and settlement within 1–3 days during downwelling events in Newfoundland coastal waters (Ings

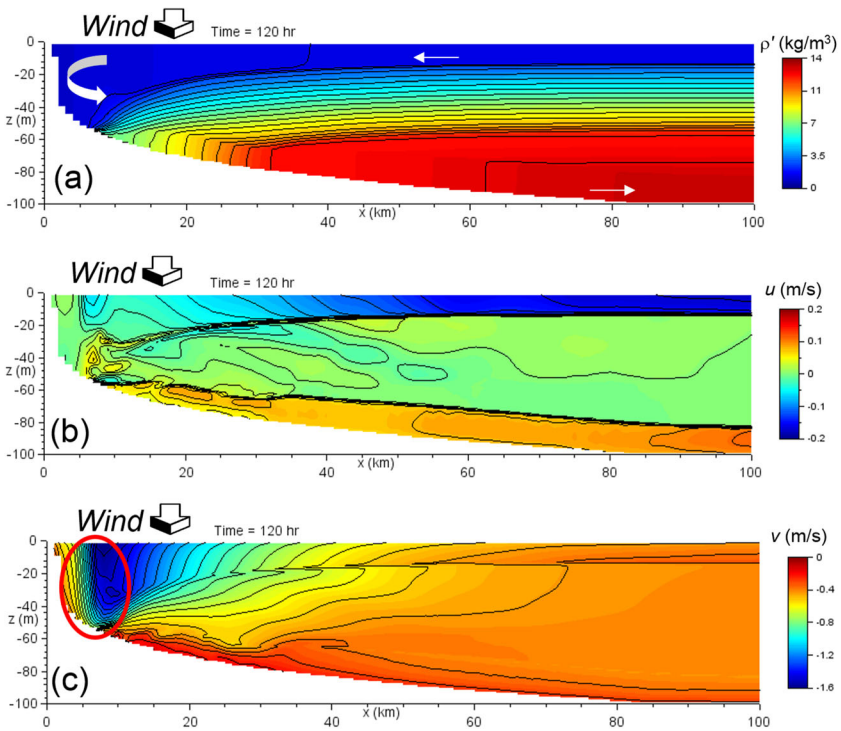

Fig. 12 Same as Fig. 6a–c, but for Experiment D-4

et al. 2008), which is no longer possible once the cross-shore circulation has weakened.

The simulated and observed shutdown of the cross-shelf circulation also explains observational evidence of larval *Tellina* spp. and *Mulinia lateralis* remaining within 5 km from the shore (i.e., the stirring zone) despite the existence of downwelling-favorable winds, while larval *Spisula solidissima* and *Ensis directus* became trapped in the near-bottom density front that developed farther offshore (Shanks and Brink 2005).

Ría de Vigo is the southernmost of four estuary-like embayments formed by the partial submergence of river valleys on the northwest Iberian coast. While the dynamics in positive estuaries have a much higher complexity than the coastal processes discussed here, it should be mentioned that Barton et al. (2016) observed the surface water subduction in conjunction with enhanced turbulence levels in the Ría de Vigo. During the downwelling, concentrations of phytoplankton increased substantially, but it remains unclear whether the downwelling event helped to recycle nutrients from the seabed in support of the phytoplankton bloom.

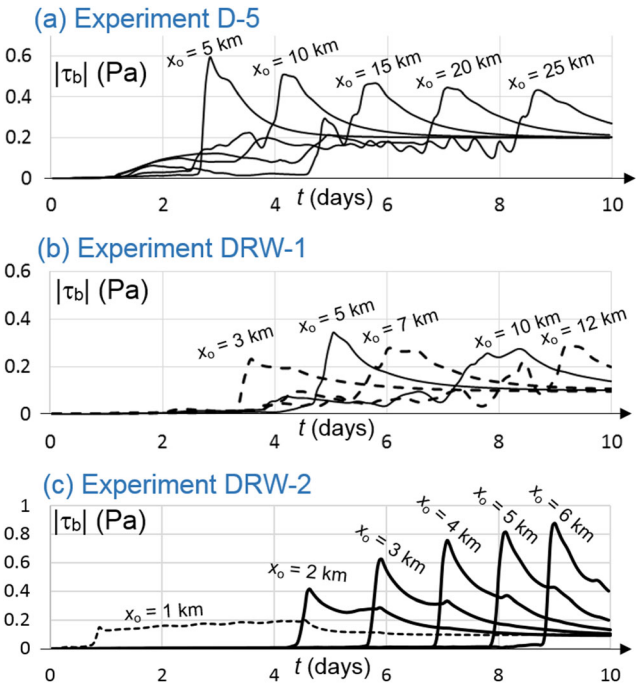

Fig. 13 Same as Fig. 11, but for different case studies (see Table 1). Note that the wind-stress magnitude is reduced from 0.2 to 0.1 Pa in experiments DRW-1 and DRW2

4 Summary and future work

This work demonstrates that downwelling-favorable winds can create extreme bed shear stresses > 0.35 Pa in a zone of intense vertical water-column stirring that may extent to distances of 20 km offshore. On the length scale of the synoptic weather patterns, such stirring zones may exist over several hundred kilometers along coastlines. In addition, it is shown the pre-existing vertical density stratification operates to enhance rather than reduce the resultant bed shear stress.

While the shutdown of the cross-shelf circulation has been reported and simulated before (e.g., Lentz 2001; Austin and Lentz 2002; Wijesekera et al. 2003; Kirincich et al. 2005),

previous studies have overlooked that such mixing episodes are accompanied by zones of extreme bed shear stresses. This significant finding may explain the high proportion of regenerated biological production in many shelf regions that relies on the ammonification of nitrogenous matter from benthic surface sediments (Herbert 1999).

It is clear that such extreme bed shear stresses have the potential to induce substantial sediment erosion and, therefore, may play an important role in sediment-transport processes in coastal oceans. It is possible that such events lead to the creation of low-density turbidity currents (e.g., Kämpf and Fohrmann 2000) or the mobilization of fluid-mud flows (e.g., Kämpf and Myrow 2018).

Unlike the upwelling process, the downwelling process cannot by easily identified from anomalies of sea surface temperatures. Given that process takes place close to shores in relatively shallow water and given that the associated sediment resuspension may be confined to sub-surface water, it is hence unclear whether satellite data can identify downwelling-related mixing episodes. Hence, more research and field work is required to further testify the significance of coastal downwelling events both for coastal ecosystems and sediment transport.

Acknowledgments The author thanks two referees for their fruitful comments and suggestions that have improved the quality of this work. All hydrodynamic model codes used in this work can be obtained from the author on request (jochen.kaempf@flinders.edu.au).

Conflict of interest The author declares that he has no competing interests.

Simplified Turbulence Closure Scheme

Description

This additional study applies the same shelf model as in the main study, but with one modification. Instead of using the k-ε scheme, vertical eddy diffusivity, A_z, is diagnosed here from Kochergin's turbulence closure (Kochergin 1987) that can be written as

$$A_z = (c\Delta z)^2 \sqrt{(\partial u/\partial z)^2 + (\partial v/\partial z)^2 - N^2} \qquad \text{(A1)}$$

where the free parameter is set to $c = 0.2$. Vertical eddy diffusivity, K_z, is again based on a turbulent Prandtl number of 0.7. The lower bound of A_z is set to a molecular value of 10^{-6} m^2/s. The upper bound of A_z is set to 0.1 m^2/s. A value of $A_z = 0.05$ m^2/s is applied near the sea surface as a representation of background wind stirring of surface water.

Note that A_z in (A1) becomes negligibly small as the gradient Richardson number (19) approaches unity. Hence, additional treatment is required to parameterize dynamic instabilities such as convective or Kelvin-Helmholtz instabilities that are expected to occur when $\mathrm{Ri_g} < 1/4$ (e.g., Baines and Mitsudera 1994; Cushman-Roisin and Beckers 2011). To account for this, the scheme is amended by the additional parameterization of effective eddy viscosity as a function of the local gradient Richardson number (e.g., Large et al. 1994; Wijesekera et al. 2003); that is;

$$A_z = \begin{cases} A_* \left[1 - \left(\mathrm{Ri_g}/\mathrm{Ri}_{cr}\right)^2\right]^3 & \text{when } 0 < \mathrm{Ri_g} < \mathrm{Ri}_{cr} \\ A_* & \text{when } \mathrm{Ri_g} < 0 \end{cases} \qquad \text{(A2)}$$

Here, we use the theoretical value of $\mathrm{Ri}_{cr} = ¼$ in conjunction with $A_* = 0.1$ m^2/s in experiment E-1 and a reduced value of $A_* = 0.01$ m^2/s in experiment E-2. Whenever $\mathrm{Ri_g} < \mathrm{Ri}_{cr}$ the value from (A2) is always used to override that from (A1). Hereby it should be firstly noted that the choice of $A_* = 0.1$ m^2/s follows from features of the mixing zone in the control experiment (see Fig. 6) and it is much larger than typically used to simulate turbulent diffusivity/viscosity in the interior of the water column ($A_* \sim 0.005$ m^2/s). Secondly, it should also be explained that purpose of reducing A_* to 0.01 m^2/s in the second experiment is to demonstrate that the high bed shear stresses developing near the downwelling front are the consequence of enhanced vertical momentum diffusion. Otherwise the experiments E-1 and E-2 are identical to the configuration of the control experiment (D-1, see Table 1).

Results

Experiment E-1 largely reproduces the results of the control experiment except for an overestimation of turbulent stirring near vertical boundaries (Appendix Fig. 14, compared with Fig. 6). This result is not unexpected given that, unlike in the k-ε scheme, the mixing length is not limited in vicinity of boundaries here. As a consequence both Ekman layers are thicker than in the control experiment. Nevertheless, all other scales are remarkable close to the control prediction, including the progression of bed shear stresses (Appendix Fig. 15, compare with Fig. 8). Again, the shelf model predicts the offshore progression of a peak bed shear stress slightly above 0.4 Pa that moves offshore at a rate of ~ 3 km per day. While experiment E-2 also predicts a similar progression due to the offshore displacement of the downwelling jet, the resultant maximum bed shear stresses are significantly smaller (Appendix Fig. 15), as least on time scales < 5 days. Hence, it is the shear instability process (induced by the cross-shelf circulation) that significantly enhanced bed shear stresses via vertical mixing of the along-shelf momentum. Quod erat demonstrandum.

High-Resolution Nonhydrostatic Simulations

Description

The shelf model used in this work cannot resolve the special scales of nonhydrostatic turbulent vortices

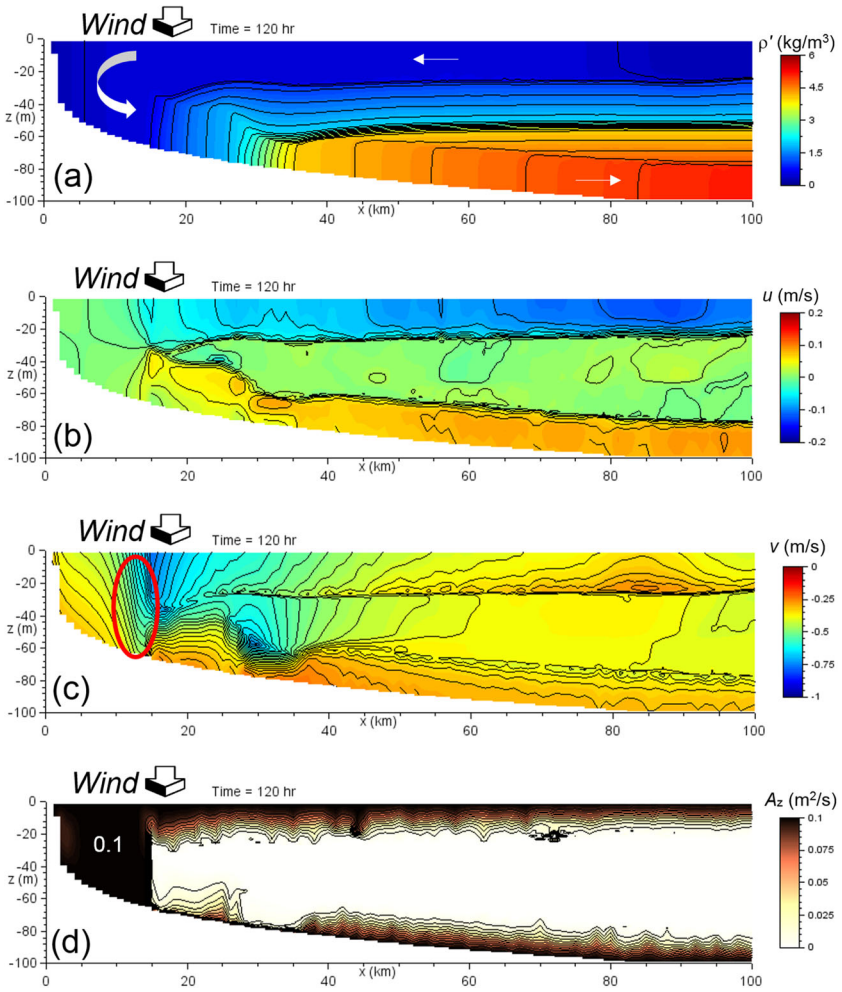

Fig. 14 Same as Fig. 6, but for experiment E-1

inherent with the Kelvin Helmholtz instability mechanism which have an aspect ratio (ratio between horizontal and vertical scales) of unity. In order to resolve those scales, the hydrodynamic equations detailed in Section 2.1.3 are applied here with a finer grid spacing of $\Delta x = \Delta z = 1$ m on a smaller horizontal spatial scale.

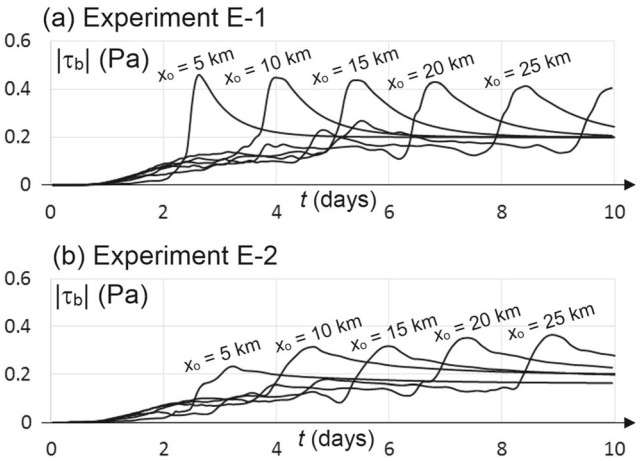

Fig. 15 Time series of bed shear stress (Pa) at selected offshore locations (x_o) for the experiments E-1 and E-2

The nonhydrostatic model is initialized by the predictions from the control experiment (D-1) using variable values for a selected single grid column (which has a horizontal width of 1 km) at a selected time. Hence, the nonhydrostatic model considers a 1-km wide model domain of a total depth corresponding to the location of the control experiment. This one-way coupling is done after every day of the "mother" simulation and at an interval of 2 km (i.e., for very second grid column of the shelf model) to an offshore distance of 30 km. Altogether this gives $10 \times 15 = 150$ simulations, but it is sufficient to only present the results of a few selected results. The total simulation time of nonhydrostatic model runs is 4 h using a numerical time step of $\Delta t = 1$ s. Initially small random fluctuations are added to the density field to seed minuscule fluctuations that can grow as part of instability processes. The vertical velocity field starts with zero values.

The nonhydrostatic assumes a flat seafloor (on the spatial scale of 1 km), and uses the same wind-stress forcing as the shelf model. Additionally the nonhydrostatic model also accounts for an external barotropic pressure-gradient force (due to the sloping surface), also prescribed from the shelf model. This pressure-gradient force is kept constant over the

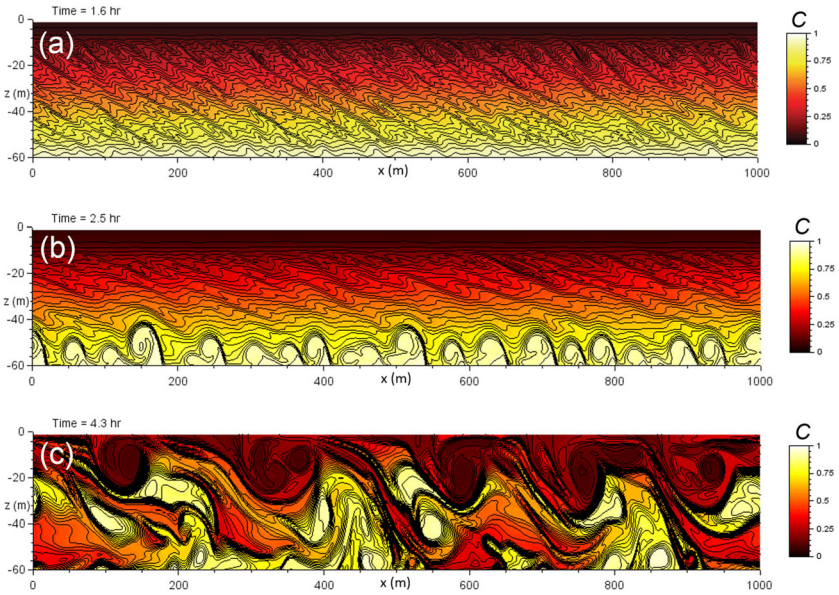

Fig. 16 Nonhydrostatic model simulation. Spatial distributions of the concentration field C after **a** 1.6 h, **b** 2.5 h, and **c** 4.3 h of simulation. The model is initialized with values from the shelf model (control experiment) at $x_o = 12$ km after 5 days of simulation

simulation period (5 h). Furthermore, the model uses cyclic horizontal boundaries, which ignores any lateral advection effects. The model also adopts Kochergin's turbulence closure but without parameterization of shear-flow and convective instabilities, which are resolved in the model. For isotropic turbulence, Kochergin's turbulence scheme can be expressed by (e.g., Kämpf and Backhaus 1998):

$$A_x = A_z = c^2(\Delta x \Delta z)^2\sqrt{(\partial u/\partial z)^2 + (\partial v/\partial z)^2 + (\partial v/\partial x)^2 + (\partial w/\partial x)^2 - N^2} \tag{B1}$$

where $c = 0.2$. In addition, a turbulent Prandt number of unity is assumed ($K_x = K_z = A_x = A_z$). The aim of this supplementary study is to test whether the vertical shear of u in conjunction with the density stratification predicted by the shelf model can initiate Kelvin-Helmholtz instabilities and, if so, whether, this mechanism leads to the predicted enhancement of bed shear stresses via modulation of v. To illustrate any stirring mechanism, the nonhydrostatic model also predicts the evolution of a passive concentration field from the advection-diffusion equation:

$$\frac{\partial}{\partial t}C + u\frac{\partial}{\partial x}C + w\frac{\partial}{\partial z}C = \frac{\partial}{\partial x}\left(K_x\frac{\partial}{\partial x}C\right) + \frac{\partial}{\partial z}\left(K_z\frac{\partial}{\partial z}C\right) \tag{B2}$$

which is of the same form as the density conservation Eq. (4). Initially, C varies linearly between zero and unity over the depth of the water column, using zero-flux vertical and cyclic lateral boundary conditions.

Results

Only results for the simulations that start from day 5 of the mother simulation are discussed here. Other start times yielded similar results. Within the stirring zone, for instance at $x_o = 12$ km (see Fig. 6), the nonhydrostatic model predicts the onset of shear-flow instabilities within 2–3 h of simulation (Appendix

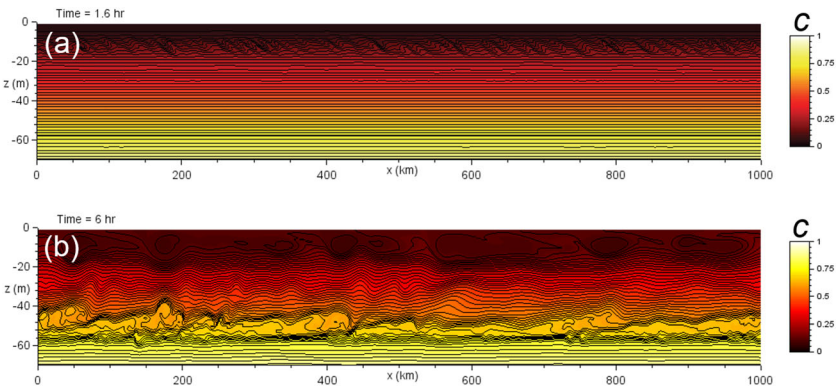

Fig. 17 Same as Appendix Fig. 16, but initialized with values from the shelf model (control experiment) at $x_o = 30$ km. Shown are the distributions of C after **a** 1.6 h and **b** 6 h of simulation

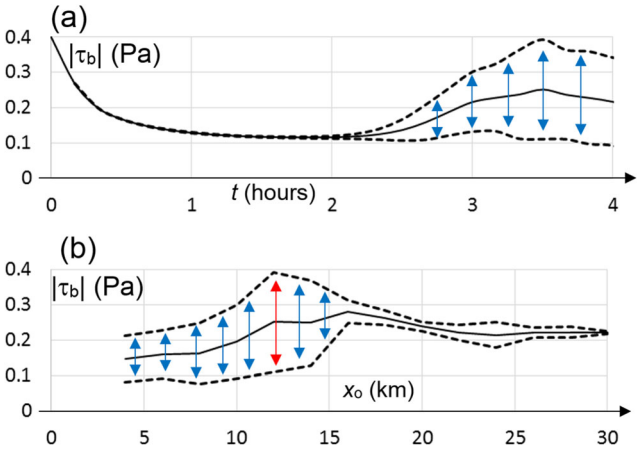

Fig. 18 Results for the nonhydrostatic model simulation that is initialized with values from the shelf model (control experiment) after 5 days of simulation. **a** Time series of bed shear stress (Pa) at $x_o = 12$ km. The solid line shows the spatial average, the dashed lines account for twice the standard deviation (i.e., 95% confidence interval). Note that the upper curve roughly corresponds to maximum bed shear stresses. **b** Resultant average and range (based on twice the standard deviation) of bed shear stresses as a function of offshore distance x_o. Arrows indicate instances in which the nonhydrostatic model predicts the onset of shear flow instabilities. The red arrow (**b**) highlights the region of peak bed shear stresses

Fig. 16). The instabilities start to develop first near the seafloor before filling the entire water column. In contrast, outside the mixing zone at $x_o = 30$ km, the pronounced density stratification near the bottom of the water column (see Fig. 6) prevents turbulence generation in vicinity of the seafloor (Appendix Fig. 17). Hence, the bed shear stress remains at moderate levels.

Appendix Fig. 18 displays the evolution of bed shear stresses at $x_o = 12$ km. Initially of bed shear stress rapidly decreases uniformly in the entire mode domain over the first hour of simulation. This decrease is caused by a modified vertical eddy viscosity that leads to a decrease of the alongshelf velocity component v near the seafloor. After the onset of dynamic instabilities, which is apparent from the increase of the standard deviation of bed shear stresses, the maximum bed shear stresses "bounce back" to reach almost the same value (~ 0.4 Pa) as simulated by the shelf model.

Simulation for other offshore locations confirm that the entire zone of apparently high vertical eddy viscosity/diffusivity (see Fig. 6d) is prone to the onset of shear-flow instabilities and vigorous mixing in the entire water column (Appendix Fig. 18). The nonhydrostatic simulations also confirm that it is the downward mixing of long-shelf momentum v that substantially enhance bed shear stresses to extremely high values.

References

Allen JS, Newberger PA (1996) Downwelling circulation on the Oregon continental shelf. Part I: response to idealized forcing. J Phys Oceanogr 26:2011–2035

Allen JS, Newberger PA, Federiuk J (1995) Upwelling circulation on the Oregon continental shelf. Part I: response to idealized forcing. J Phys Oceanogr 25:1843–1866

Austin JA, Lentz SJ (2002) The inner shelf response to winddriven upwelling and downwelling. J Phys Oceanogr 22:2171–2193

Baines PG, Mitsudera H (1994) On the mechanism of shear flow instabilities. J Fluid Mech 276:327–342

Barton ED, Torres R, Figueiras FG, Gilcoto M, Largier J (2016) Surface water subduction during a downwelling event in a semi-enclosed bay. J Geophys Res-Oceans 121:7088–7107. https://doi.org/10.1002/2016JC011950

Burchard H, Petersen O, Rippeth TP (1998) Comparing the performance of the Mellor–Yamada and the k-ε two-equation turbulence models. J Geophys Res 103:10543–10554

Campin J-M, Hill C, Jones H, Marshall J (2011) Super-parameterization in ocean modeling: application to deep convection. Ocean Mod 36(1–2):90–101. https://doi.org/10.1016/j.ocemod.2010.10.003

Chang GC, Dickey TD, Williams AJ III (2001) Sediment resuspension over a continental shelf during hurricanes Edouard and Hortense. J Geophys Res 106:9517–9531

Churchill JH, Wirick CD, Flagg CN, Pietrafesa LJ (1994) Sediment resuspension over the continental shelf east of the Delmarva Peninsula. Deep-Sea Res II Top Stud Oceanogr 41:341–363

Cushman-Roisin B, Beckers J-M (2011) Introduction to geophysical fluid dynamics. Academic Press, Cambridge

de Szoeke RA, Richman R (1984) On wind-driven mixed layers with strong horizontal gradients—a theory with application to coastal upwelling. J Phys Oceanogr 14:364–377

Drazin PG, Reid WH (1981) Hydrodynamic stability. Cambridge University Press, Cambridge

Ekman VW (1905) On the influence of the earth's rotation on ocean-currents. Ark Mat Astr Fys 2(11):1–53

Eppley RW, Peterson BJ (1979) Particulate organic flux and planktonic new production in the deep ocean. Nature 282:677–680

Fanning KA, Carder KL, Betzer PR (1982) Sediment resuspension by coastal waters: a potential for nutrient re-cycling on the oceans margins. Deep Sea Res 29:953–965

Fennel W (1999) Theory of the Benguela upwelling system. J Phys Oceanogr 29(2):177–190

Greenwood B, Osborne PD (1990) Vertical and horizontal structure in cross-shore flows: an example of undertow and wave set-up on a barred beach. Coast Eng 14:543–580

Hansen LS, Blackburn TH (1992) Effect of algal bloom deposition on sediment respiration rates and fluxes. Mar Biol 112:147–152

Hela I (1976) Vertical velocity of the upwelling in the sea. Soc Sci Fennicia Commentationes Phys Math 46:9–24

Herbert RA (1999) Nitrogen cycling in coastal marine ecosystems. FEMS Microbial Rev 23:563–590

Ings DW, Gregory RS, Schneider DC (2008) Episodic downwelling predicts recruitment of Atlantic cod, Greenland cod and white hake to Newfoundland coastal waters. J Mar Res 66(4):529–561. https://doi.org/10.1357/002224008787157476

Jensen HM, Lomstein E, Sorensen J (1990) Benthic NH_4 and NO_3 fluxes following sedimentation of a spring phytoplankton bloom in Aarhus bight, Denmark. Mar Ecol Prog Ser 61:87–96

Kämpf J (2009) Ocean modelling for beginners. Springer, Heidelberg

Kämpf J (2010) Advanced ocean modelling. Springer, Heidelberg

Kämpf J (2015) Interference of wind-driven and pressure gradient-driven flows in shallow homogeneous water bodies. Ocean Dyn 65(11):1399–1410. https://doi.org/10.1007/s10236-015-0882-2

Kämpf J (2017) Wind-driven overturning, mixing and upwelling in shallow water: a nonhydrostatic modeling study. J Mar Sci Eng 5:47. https://doi.org/10.3390/jmse5040047

Kämpf J, Backhaus JO (1998) Shallow, brine-driven free convection in polar oceans: nonhydrostatic numerical process studies. J Geophys Res 103:5577–5593

Kämpf J, Chapman P (2016) Upwelling systems of the world: a scientific journal to the most productive marine ecosystems. Springer International Publishing, Cham

Kämpf J, Fohrmann H (2000) Sediment-driven downslope flow in submarine canyons and channels: three-dimensional numerical experiments. J Phys Oceanogr 30(9):2302–2319

Kämpf J, Myrow PM (2018) Wave-created mud suspensions: a theoretical study. J Mar Sci Eng 6(2):29. https://doi.org/10.3390/jmse6020029

Kirincich AR, Barth JA, Grantham BA, Menge BA, Lubchenco J (2005) Wind-driven inner-shelf circulation off central Oregon during summer. J Geophys Res 110:C10S03. https://doi.org/10.1029/2004JC002611

Kochergin VP (1987) Three-dimensional prognostic models. In: Heaps NS (ed) Three-dimensional coastal ocean models, coastal estuarine science series 4. American Geophysical Union, Washington, pp 201–208

Kuzmin D, Mierka O, Turek S (2007) On the implementation of the k-ε turbulence model in incompressible flow solvers based on a finite element discretization. Int J Comput Sci Math 1(2–4):193–206

Large WG, McWilliams JC, Doney SC (1994) Oceanic vertical mixing: a review and a model with a nonlocal boundary layer parameterization. Rev Geophys 32:363–403

Laws EA (2004) New production in the equatorial Pacific: a comparison of field data with estimates derived from empirical and theoretical models. Deep-Sea Res I 51:205–211

Lentz SJ (2001) The influence of stratification on the wind-driven cross-shelf circulation over the North Carolina shelf. J Phys Oceanogr 31:2749–2760

Lettmann KA, Wolff J-O, Badewien TH (2009) Modeling the impact of wind and waves on suspended particulate matter fluxes in the east Frisian Wadden Sea (southern North Sea). Ocean Dyn 59(2):239–262. https://doi.org/10.1007/s10236-009-0194-5

McCreary J, Kundu PK (1985) Western boundary circulation driven by an alongshore wind: with application to the Somali current system. J Mar Res 43:493–516

Mitchener H, Torfs H, Whitehouse R (1996) Erosion of mud/sand mixtures. Coast Eng 29:1–25

Moum JN, Perlin A, Klymak JM, Levine MD, Boyd T, Kosro PM (2004) Convectively-driven mixing in the bottom boundary layer over the continental shelf during downwelling. J Phys Oceanogr 34:2189–2202. https://doi.org/10.1175/1520-0485(2004)034<2189:CDMITB>2.0.CO;2

Nixon SW (1981) Remineralisation and nutrient cycling in coastal marine ecosystems. In: Nielson BJ, Cronin LE (eds) Estuaries and nutrients. Humana Press, New Jersey, pp 111–138

Rodi W (1987) Examples of calculation methods for flow and mixing in stratified fluids. J Geophys Res 92(C5):5305–5328

Schloen J, Stanev EV, Grashorn S (2017) Wave-current interactions in the southern North Sea: the impact on salinity. Ocean Model 111:19–37

Shanks AL, Brink L (2005) Upwelling, downwelling, and cross-shelf transport of bivalve larvae: test of a hypothesis. Mar Ecol Prog Ser 302:1–12

Stanev EV, Dobrynin M, Pleskachevsky A, Grayek S, Günther H (2009) Bed shear stress in the southern North Sea as an important driver for suspended sediment dynamics. Ocean Dyn 59(2):183–194. https://doi.org/10.1007/s10236-008-0171-4

Tilburg CE (2003) Across-shelf transport on a continental shelf: do across-shelf winds matter? J Phys Oceanogr 33:2675–2688

Wijesekera HW, Allen JS, Newberger PA (2003) Modeling study of turbulent mixing over the continental shelf: comparison of turbulent closure schemes. J Geophys Res 108(C3):3103. https://doi.org/10.1029/2001JC001234